nature physics

Article

https://doi.org/10.1038/s41567-024-02444-w

Manipulation of chiral interface states in a moiré quantum anomalous Hall insulator

Received: 14 July 2023

Accepted: 16 February 2024

Published online: 13 March 2024

Check for updates

Canxun Zhang[1,2,3,6,8], Tiancong Zhu[1,2,7,8] ✉, Salman Kahn[1,2,8], Tomohiro Soejima[1], Kenji Watanabe[4], Takashi Taniguchi[5], Alex Zettl[1,2,3], Feng Wang[1,2,3], Michael P. Zaletel[1,2] & Michael F. Crommie[1,2,3] ✉

Moiré systems made from stacked two-dimensional materials host correlated and topological states that can be electrically controlled with applied gate voltages. One prevalent form of topological state that can occur are Chern insulators that display a quantum anomalous Hall effect. Here we manipulate Chern domains in an interaction-driven quantum anomalous Hall insulator made from twisted monolayer–bilayer graphene and observe chiral interface states at the boundary between different domains. By tuning the carrier concentration, we stabilize neighbouring domains of opposite Chern number that then provide topological interfaces devoid of any structural boundaries. This allows the wavefunction of chiral interface states to be directly imaged using a scanning tunnelling microscope. Our theoretical analysis confirms the chiral nature of observed interface states and allows us to determine the characteristic length scale of valley polarization reversal across neighbouring Chern domains.

van der Waals stacks of two-dimensional (2D) atomic sheets provide a versatile platform for exploring topologically non-trivial phases of matter. The formation of moiré superlattices owing to rotational misalignment or lattice mismatch induces energetically narrow mini-bands[1–3] that inherit the large Berry curvature of the individual atomic layers[4–6]. Spontaneous valley polarization in the presence of strong electron–electron interactions can break the time reversal symmetry, leading to a variety of topological states such as quantum anomalous Hall (QAH) insulators[7–9], fractional Chern insulators[10–14] and topological charge density waves[15]. The non-trivial topology and associated magnetic order of these moiré systems can be manipulated via electrical means without high magnetic field[7,8,16,17], thus promising exciting applications ranging from ultra-low-power magnetic memories[8] to topological quantum computation[18–20]. The microscopic mechanisms at work in these materials and their ultimate performance in future applications, however, depend sensitively on spatial characteristics of chiral interface states that up to now have proved difficult to visualize owing to extrinsic factors such as structural defects.

In this Article, we describe the use of scanning tunnelling microscopy (STM)/scanning tunnelling spectroscopy (STS) to manipulate Chern domains and to directly visualize the wavefunction of chiral interface states in a moiré QAH insulator made from twisted monolayer–bilayer graphene (tMBLG). Neighbouring tMBLG domains were induced to exhibit opposite Chern number by tuning the electron density in our devices via electrostatic gating. Spatially resolved STS was used to visualize topological phase transitions across the interfaces between such domains and to directly probe the local electronic structure of resulting one-dimensional (1D) chiral modes. We have discovered that these 1D chiral states can be spatially displaced on demand via global back-gating. Moreover, we are able to create interface states with predetermined chirality and position via tip-pulse-induced quantum dot formation[21]. Comparison of our data with an effective theoretical

[1]Department of Physics, University of California, Berkeley, CA, USA. [2]Materials Sciences Division, Lawrence Berkeley National Laboratory, Berkeley, CA, USA. [3]Kavli Energy NanoScience Institute, University of California, Berkeley and the Lawrence Berkeley National Laboratory, Berkeley, CA, USA. [4]Research Center for Electronic and Optical Materials, National Institute for Materials Science, Tsukuba, Japan. [5]Research Center for Materials Nanoarchitectonics, National Institute for Materials Science, Tsukuba, Japan. [6]Present address: Department of Physics, University of California, Santa Barbara, CA, USA. [7]Present address: Department of Physics and Astronomy, Purdue University, West Lafayette, IN, USA. [8]These authors contributed equally: Canxun Zhang, Tiancong Zhu, Salman Kahn. ✉e-mail: zhu1242@purdue.edu; crommie@berkeley.edu

https://doi.org/10.1038/s41567-024-02444-w

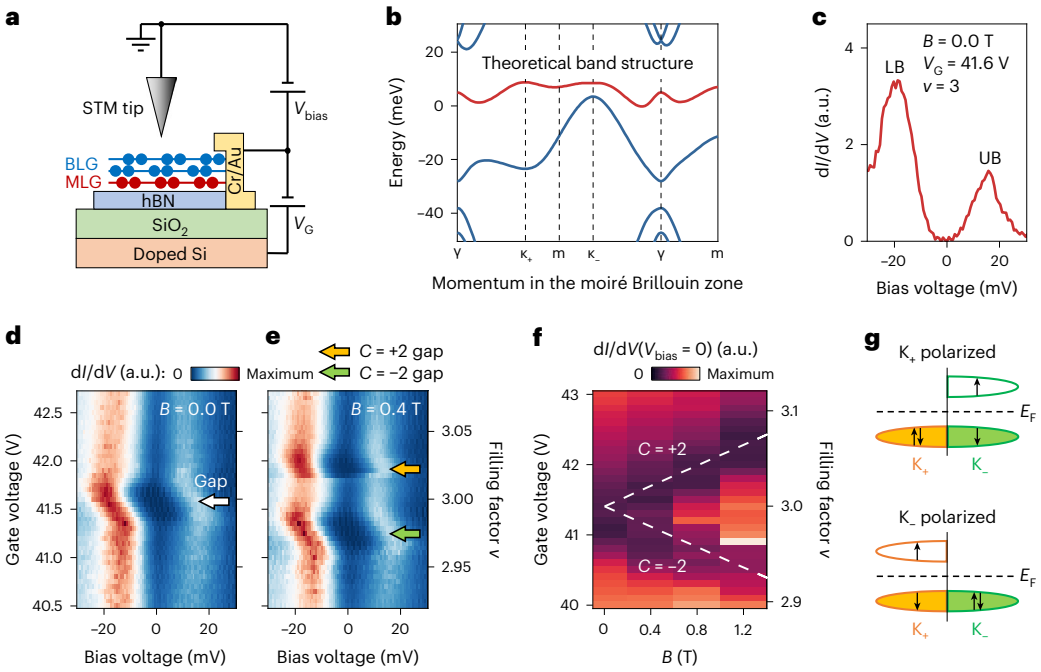

Fig. 1 | Local characterization of gate-tuneable Chern number for tMBLG QAH states. a, A sketch of the tMBLG device in the STM/STS measurement geometry. MLG, monolayer graphene; BLG, Bernal-stacked bilayer graphene. There is a twist angle between MLG and BLG. **b**, The single-particle band structure of $\theta = 1.25°$ tMBLG along the high-symmetry directions of the moiré Brillouin zone. For clarity, only mini-bands from the unfolded K_+ valley are shown. **c**, The dI/dV spectrum obtained in an area with a local twist angle of 1.25° for $B = 0.0$ T and $V_G = 41.6$ V ($\nu = 3$). This is the same area as shown in Extended Data Fig. 1. **d**, The gate-dependent dI/dV for tMBLG near $\nu = 3$ ($B = 0.0$ T). The white arrow indicates the energy gap. **e**, The same as **d** but at $B = 0.4$ T. Orange and green arrows indicate $C = +2$ and $C = -2$ gaps. **f**, dI/dV($V_{bias} = 0$) as a function of V_G and the B field for tMBLG (see Extended Data Fig. 2a–d for additional details). Dashed lines show the Středa formula for $C = \pm 2$. **g**, A schematic of the tMBLG band filling for the unfolded K_+ valley-polarized state (top) and K_- valley-polarized state (bottom) at $\nu = 3$. Arrows represent electron spin. The experimental spectroscopy parameters were modulation voltage $\Delta V_{RMS} = 1$ mV, setpoint $V_{bias} = -60$ mV and $I_0 = 0.5$ nA. All measurements were taken at $T = 4.7$ K.

model confirms that chiral interface states arise in tMBLG owing to a reversal of valley polarization across Chern domains and allows us to determine the characteristic width of a Chern domain wall. This length scale has substantial implications for the microscopic origin of spatially defined topological phase transitions as well as potential device applications.

Density control of local tMBLG Chern number

Figure 1a shows a sketch of our experiment, which incorporates a tMBLG device within an STM measurement geometry. Here, Bernal-stacked bilayer graphene is placed on top of a monolayer graphene with a twist angle $\theta \approx 1.25°$ between them, and the stack is supported by a hexagonal boron nitride (hBN) substrate placed on an Si/SiO_2 wafer that functions as the back gate (Methods). The monolayer–bilayer rotational misalignment generates a moiré superlattice of wavelength $l_M \approx 11.3$ nm (Methods and Extended Data Fig. 1a) that folds dispersive electronic bands into energetically narrow mini-bands, each accommodating four electrons per moiré unit cell due to spin and valley degeneracies (Fig. 1b)[22,23]. Tuning the back-gate voltage V_G allows us to dope the graphene stack with charge carriers that partially occupy the moiré mini-band electronic states (Extended Data Fig. 1b). At integer filling factors ν (defined as the average number of electrons per moiré unit cell referenced to charge neutrality; Supplementary Note 1), strong electron–electron interactions can induce correlated insulating states that lift the spin/valley degeneracy. Figure 1c shows a representative differential conductance (dI/dV) spectrum obtained at $V_G = 41.6$ V ($\nu = 3$) where a charge gap with nearly vanishing dI/dV appears around $V_{bias} = 0$ mV (that is, the Fermi energy E_F), flanked by a lower band (LB) peak and an upper band (UB) peak.

This $\nu = 3$ insulating state exhibits non-trivial topological behaviour, as shown by the QAH effect reported in previous transport measurements[8]. We are able to directly observe its topological properties via STM by performing gate-dependent dI/dV spectroscopy in an applied out-of-plane magnetic field B (ref. 24). Figure 1d shows a dI/dV density plot for $B = 0.0$ T, where the $\nu = 3$ gap is marked by a white arrow. Under application of a small magnetic field ($B = 0.4$ T), this gap evolves into two separate gaps that exhibit similar spectroscopic features but are situated at different electron densities, one above and one below $\nu = 3$ (Fig. 1e, orange and green arrows). These two gaps split further away from $\nu = 3$ with increasing B, as shown by the V-shaped dark region in the dI/dV density plot obtained at $V_{bias} = 0$ mV (Fig. 1f; see Extended Data Fig. 2 for additional details). Such linear scaling between gap position and B field is indicative of a QAH insulating state whose Chern number is either $C = +2$ (for the $\nu > 3$ branch) or $C = -2$ (for the $\nu < 3$ branch), as extracted from the Středa formula $\frac{\Delta n}{\Delta B} = \frac{C}{\Phi_0}$ (ref. 25; n is the carrier density and Φ_0 is the magnetic flux quantum). This separation of $C = \pm 2$ states allows us to independently access different Chern states in a small B field by tuning the electron density via electrostatic gating, thus providing electrical control over the local Chern number in our tMBLG device.

Topological phase transition and chiral interface states

Electrical control over the tMBLG Chern number provides us with a unique opportunity to stabilize neighbouring insulating domains with opposite local Chern values and to explore the topological phase transition across them in regions exhibiting charge inhomogeneity. Figure 2a shows an STM topographic image of such an area in tMBLG having a relatively uniform local twist angle of $\theta = 1.25 \pm 0.01°$ and a local hetero-strain between 0.1% and 0.2% (Extended Data Fig. 3a). Spatial inhomogeneity in the charge density is reflected in the dI/dV density plots of Fig. 2b for $B = 0.0$ T, where the $\nu = 3$ gap (white arrows) occurs at different V_G values for locations 1–3. Application of an out-of-plane field $B = 0.4$ T causes the $\nu = 3$ gap to evolve into two gaps of opposite Chern number (Fig. 2c), with the charge inhomogeneity causing the gaps to occur at different gate voltages at different locations. At $V_G = 42.0$ V (Fig. 2c,

https://doi.org/10.1038/s41567-024-02444-w

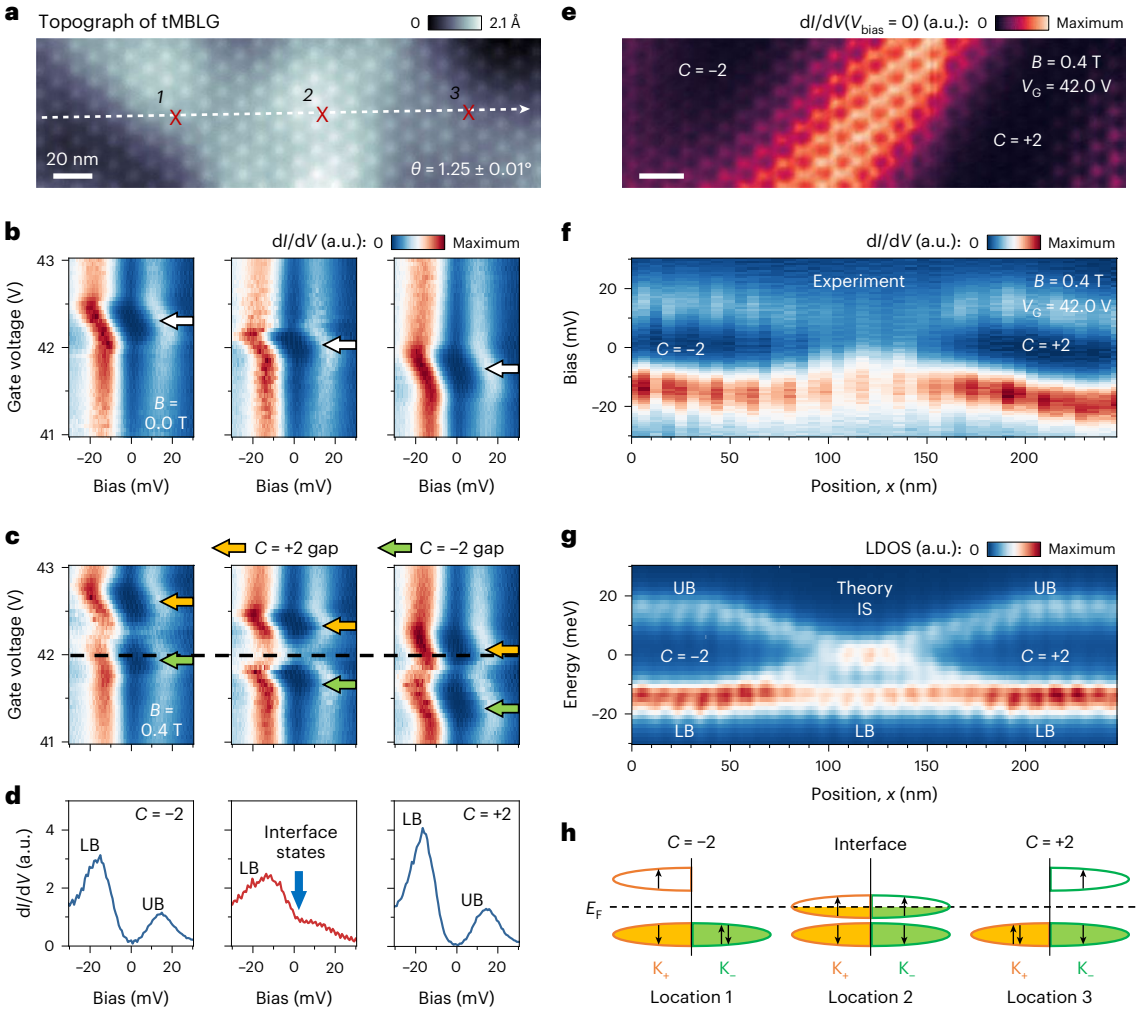

Fig. 2 | Topological phase transition and 1D chiral states at a Chern domain interface. a, An STM topographic image of a tMBLG area having inhomogeneous electron density (V_{bias} = −300 mV and setpoint I_0 = 0.2 nA). **b**, Gate-dependent dI/dV density plots for B = 0.0 T obtained at locations 1 (left), 2 (middle) and 3 (right) in **a**. White arrows indicate the ν = 3 energy gap. **c**, The same as **b** but for B = 0.4 T. Orange and green arrows indicate C = +2 and C = −2 gaps. **d**, dI/dV spectra for B = 0.4 T and V_G = 42.0 V taken at locations 1, 2 and 3 in **a**. **e**, dI/dV map of the same area as **a** for B = 0.4 T, V_G = 42.0 V and V_{bias} = 0 mV. The bright region shows the chiral interface state density. **f**, A dI/dV density plot for B = 0.4 T and V_G = 42.0 V, obtained along the white dashed line in **a**. **g**, The theoretical LDOS calculated for a Chern domain wall width of ξ = 125 nm for comparison with **f**. IS, interface states. **h**, A schematic band diagram for the topological phase transition across a tMBLG Chern domain interface. Arrows represent electron spin. The experimental spectroscopy parameters were modulation voltage ΔV_{RMS} = 1 mV, setpoint V_{bias} = −60 mV and I_0 = 0.5 nA for **b** and **c** and setpoint V_{bias} = −300 mV, I_0 = 0.2 nA and tip height offset ΔZ = −0.075 nm for **d**–**f**.

dashed line), location 1 acquires the lower gap (left panel), indicating that it is in a C = −2 insulating domain, whereas location 3 acquires the higher gap (right panel), indicating that it is in a C = +2 insulating domain.

To visualize the tMBLG local electronic structure between insulating domains of opposite Chern number, Fig. 2f shows dI/dV spectra obtained along the dashed white line in Fig. 2a (representative point spectra are shown in Fig. 2d). A gap feature is clearly seen in the far left (x < 80 nm) and far right (x > 160 nm) regions, along with the LB and UB peaks. The spectra in the middle region (80 nm < x < 160 nm), however, exhibit very different behaviour. The LB peak persists (with reduced intensity), but the UB peak can no longer be clearly resolved. Moreover, an increase in the dI/dV signal emerges at V_{bias} = 0 mV (that is, E_F) that closes the insulating gap (as seen in the middle dI/dV spectrum in Fig. 2d as well as Extended Data Fig. 4c). These data are the signature of a real-space topological phase transition that starts in a C = −2 insulating domain and progresses through a conducting interface to a C = +2 insulating domain. It is important to note that the tMBLG region at the interface between these two Chern domains is unblemished and exhibits no structural defects.

The presence of a conducting region at the Chern domain interface is consistent with the emergence of 1D chiral modes between QAH insulators having different Chern numbers. The microscopic wavefunction of such modes can be seen in Fig. 2e through a dI/dV map taken at V_{bias} = 0 mV of the same area as in Fig. 2a (for V_G = 42.0 V and B = 0.4 T; Methods). The C = −2 and C = +2 domains in Fig. 2e appear as dark regions with nearly vanishing dI/dV, whereas the bright stripe in the middle is a visualization of the 1D chiral interface modes (that extend diagonally from the lower left to the upper right). Similar spatially defined topological phase transitions (accompanied by chiral interface states) were observed in numerous different tMBLG areas having inhomogeneous electron density (Extended Data Fig. 5). The 2D Gaussian fit profiles made for zero-bias dI/dV maps at four different topological interfaces result in a full-width at half-maximum (FWHM) for tMBLG chiral interface modes equal to 57 ± 10 nm (Methods and Extended Data Fig. 6).

Manipulating interface states with electrostatic gating

The emergence of Chern domains and chiral interface states in tMBLG that are sensitive to local electron density (but independent of structural boundaries) allows flexible manipulation of their spatial location

https://doi.org/10.1038/s41567-024-02444-w

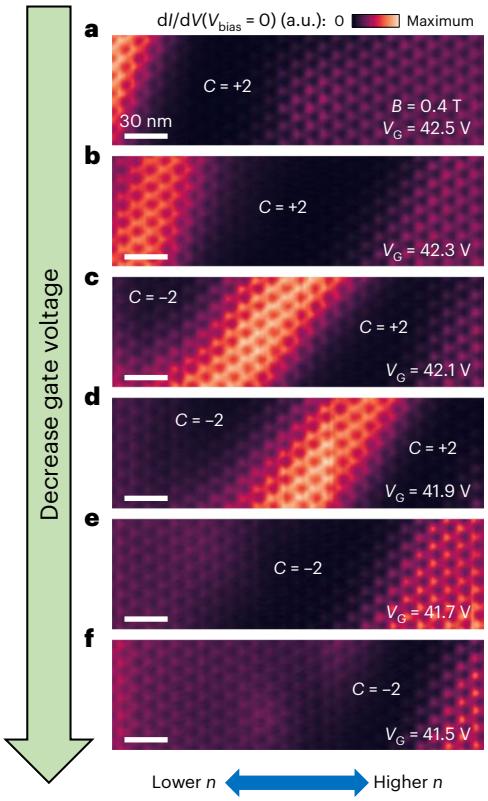

Fig. 3 | Manipulating Chern domains and chiral interface states via back-gating. a–f, dI/dV maps of the same area shown in Fig. 2a at $B = 0.4$ T and $V_{bias} = 0$ mV for $V_G = 42.5$ V (**a**), $V_G = 42.3$ V (**b**), $V_G = 42.1$ V (**c**), $V_G = 41.9$ V (**d**), $V_G = 41.7$ V (**e**) and $V_G = 41.5$ V (**f**). The experimental spectroscopy parameters were modulation voltage $\Delta V_{RMS} = 1$ mV, setpoint $V_{bias} = -300$ mV, $I_0 = 0.2$ nA and tip height offset $\Delta Z = -0.075$ nm.

via electrostatic back-gating. Figure 3 shows a series of zero-bias dI/dV maps of the same chiral interface modes as shown in Fig. 2e as V_G is gradually decreased from 42.5 to 41.5 V (the region on the right has a higher local electron density n than the left region). At $V_G = 42.5$ V (Fig. 3a), the electron density is above $\nu = 3$ for the entire scanned area. The darkest region on the left side is in the $C = +2$ insulating state (that is, dI/d$V \approx 0$), whereas the region on the right side has some additional electron doping that results in dI/d$V > 0$. Decreasing V_G (Fig. 3b) reduces the local electron density everywhere, causing the $C = +2$ insulating domain to shift towards the right (that is, according to the gradient shown in Fig. 2c). At $V_G = 42.1$ V, the left region switches to a $C = -2$ insulating state and the right region exhibits a $C = +2$ state, and bright 1D states remain at the interface between them (Fig. 3c). Further decreasing V_G leads to expansion of the $C = -2$ domain and reduction of the $C = +2$ domain, moving the interface states continuously from left to right (Fig. 3d,e). Finally, at $V_G = 41.5$ V, the entire scanned area lies below $\nu = 3$ with the darkest region on the right side representing a $C = -2$ insulating state and the region to its left being slightly hole doped (Fig. 3f). This interface state manipulation process is completely reversible as V_G is increased back to 42.5 V (Extended Data Fig. 7).

Creating interface states with reversible chirality

We are able to create chiral interface states by design by inducing charge inhomogeneity through STM tip-pulse-induced quantum dots. Figure 4a shows an area of a tMBLG device having a nearly uniform local twist angle of $\theta = 1.26 \pm 0.01°$ and relatively low variation of the local electron density n in its pristine state (see Extended Data Figs. 3b and 8b for additional details). To alter the density profile, we applied a bias voltage pulse of 5 V at the location marked by the red dot in Fig. 4a while holding the gate voltage fixed at $V_G = -2$ V (Fig. 4b). This process changes the charge state of defects in the hBN substrate, resulting in an n-type (that is, electron-doped) graphene quantum dot centred at the site of the bias pulse[21] (see Supplementary Note 2 and Extended Data Fig. 8c for additional details). Under these conditions, the tMBLG electron density decreases away from the dot centre, thus causing a density gradient that induces a Chern domain interface and chiral interface states near the dot edge, as described previously in Fig. 2.

Chiral interface states created in this way can be identified using STS, as shown in Fig. 4c. Under the application of $B = 0.4$ T and $V_G = 43.0$ V, the location marked '1' in Fig. 4a is found to be in the gapped $C = +2$ state (Fig. 4c, left) while the location marked '3' (which has lower local n) is found to be in the gapped $C = -2$ state (Fig. 4c, right). The location between these two points (marked '2' in Fig. 4a) shows a collapse of the energy gap and thus indicates the position of new chiral interface states (Fig. 4c, middle; see Extended Data Fig. 9a–c for additional details). Such chiral states propagate unidirectionally according to the Chern number difference across the interface, so one can deduce that electrons must flow downwards along this interface on the basis of the Chern numbers of the neighbouring domains (Fig. 4d).

The chirality (and thus the direction of electron flow) for these tailor-made interface states can be flipped by reversing the polarity of the quantum dot. To accomplish this, we applied a bias voltage pulse of 5 V to the same location in Fig. 4a as before while holding $V_G = +2$ V as shown in Fig. 4e. This erased the previous quantum dot and induced a p-type (that is, hole-doped) graphene quantum dot in the same area, thus reversing the electron density gradient in regions 1–3. Under the application of $B = 0.4$ T and $V_G = 45.0$ V, a gapped $C = -2$ domain is now observed at location 1 (Fig. 4f, left) and a gapped $C = +2$ domain is observed at location 3 (Fig. 4f, right). Location 2 (Fig. 4f, middle) shows a collapse of the energy gap and thus marks the location of newly formed chiral interface modes, but now with the difference that the domain Chern numbers are reversed and thus the electron flow is flipped (Fig. 4g). The chirality of artificially fabricated interface modes can thus be switched (see Extended Data Fig. 9d–f for additional details).

Theoretical model and discussion

The behaviour that we observe for Chern domains and chiral interface states in tMBLG can be understood by analysing the origin of the non-trivial topology of interaction-driven insulating states. The tMBLG moiré mini-band investigated in our experiment (Fig. 1b, red) is fourfold degenerate, with each sub-band originating from an unfolded K_+ or K_- valley having a non-zero Chern number of $c(K_\pm) = \pm 2$ owing to the large Berry curvature inherited from the constituent graphene layers[22,23]. At $\nu = 3$, strong Coulomb exchange interactions induce spontaneous polarization in the spin–valley space, with three of the four spin- and valley-resolved sub-bands becoming filled (corresponding to the experimental LB peak in Fig. 1c) and the remaining one being empty (corresponding to the experimental UB peak in Fig. 1c). This leads to a time reversal symmetry-broken insulating state with a total Chern number $C \neq 0$ due to unbalanced electron occupation between the two valleys (Fig. 1g)[8,24]. Double occupancy in the K_+ valley and single occupancy in the K_- valley results in a gapped $C = +2$ state (Fig. 1g, top), whereas the opposite configuration leads to a $C = -2$ state (Fig. 1g, bottom).

Neighbouring $C = +2$ and $C = -2$ insulating domains as observed in our experiment correspond to opposite valley occupancies, so valley polarization reversal is expected across the domain interface. The simplest scenario for such a transition is illustrated in Fig. 2h. As one moves from the $C = -2$ domain (location 1) to the $C = +2$ domain (location 3), the empty K_+ sub-band smoothly shifts downwards in energy and becomes occupied, while a filled K_- sub-band smoothly shifts upwards and becomes depleted. This qualitative picture leads to a closing (location 2) and reopening (location 3) of the correlation

https://doi.org/10.1038/s41567-024-02444-w

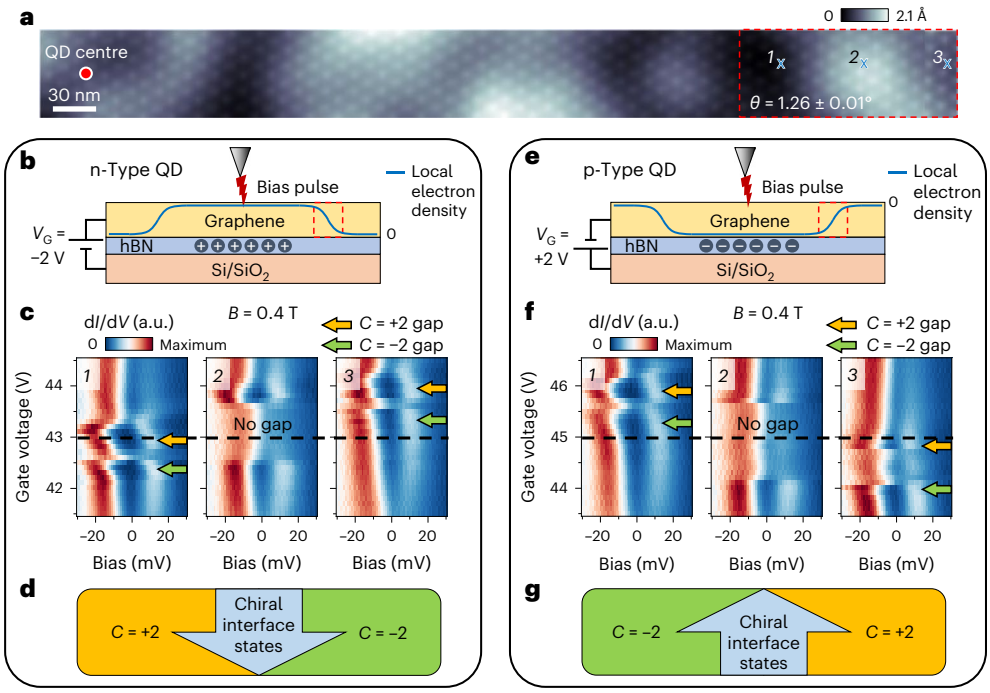

Fig. 4 | Creating chiral interface states with tuneable chirality via STM tip-pulse-induced quantum dots. a, An STM topographic image of a tMBLG area after using an STM tip pulse to create a quantum dot ($V_{bias} = -1$ V and setpoint $I_0 = 0.01$ nA). **b**, A schematic of the process of inducing an n-type quantum dot (QD). The blue curve signifies the resulting graphene quantum dot local electron density. The dashed red box highlights the region with the largest density gradient and represents the boxed region in **a**. **c**, dI/dV density plots for $B = 0.4$ T obtained at locations 1, 2 and 3 in **a** after the creation of an n-type quantum dot centred at the red dot in **a** (modulation voltage $\Delta V_{RMS} = 1$ mV, setpoint $V_{bias} = -60$ mV and $I_0 = 0.5$ nA). Orange and green arrows indicate $C = +2$ and $C = -2$ energy gaps. Discontinuities in spectroscopic features as a function of V_G probably arise from abrupt depinning of the domain interface (Supplementary Note 3). **d**, An illustration of the region encircled by the dashed red box in **a** for the case of an n-type quantum dot with $B = 0.4$ T and $V_G = 43.0$ V (that is, corresponding to the horizontal dashed line in **c**). The blue arrow shows the direction of electron flow for chiral interface states. **e**, A schematic of the process of inducing a p-type QD. **f**, The same as **c**, but after the creation of a p-type quantum dot centred at the red dot in **a**. **g**, The same as **d** except for the case of a p-type quantum dot with $B = 0.4$ T and $V_G = 45.0$ V (that is, corresponding to the horizontal dashed line in **f**). Note that the direction of the blue arrow is reversed compared with **d**.

gap across the domain interface, as observed experimentally (Fig. 2f). At the interface, both a K_+ sub-band and a K_- sub-band are partially occupied, which leads to 1D conducting states at E_F.

Such a picture of valley polarization reversal allows us to construct a quantitative model of tMBLG Chern domain interfaces that enables the extraction of useful physical parameters from the chiral interface states observed in our experiment. Here, the moiré mini-band is described by a tight-binding model derived from a continuum Hamiltonian[22,23], and the correlation-induced valley polarization and reversal is modelled using a spatially varying energy offset (Supplementary Note 4). In the bulk of each insulating domain, we assume an energy separation of $2E_0 = 30$ meV between occupied and unoccupied electronic states as extracted from the experimental dI/dV (Fig. 2d,f). Starting from a $C = -2$ domain and moving towards a $C = +2$ domain, the downwards-shifting K_+ sub-band is first centred at $+E_0$ (Fig. 2h, location 1) and ends up centred at $-E_0$ (location 3). As the interface is crossed, the energy offset shifts linearly from $+E_0$ to $-E_0$ over a valley domain wall width of ξ that depends on details of the electron–electron interaction and the local carrier density profile. The energy offset for the upwards-shifting K_- sub-band has the opposite spatial profile. Solving for the electronic eigenstates of this model yields four 1D branches that span the bulk gap and disperse unidirectionally (Extended Data Fig. 10a,c), thus confirming the emergence of chiral interface modes residing between the $C = -2$ and $C = +2$ insulating domains.

Using this model, we are able to reproduce the spatially dependent topological phase transition that we observe experimentally as the interface is crossed and to explain the origin of the different features seen in our STM spectroscopy. Figure 2g shows the resulting theoretical local density of states (LDOS) across the domain interface for $\nu = 3$ and $\xi = 125$ nm. Here, ξ is the only parameter not fixed by experiment and $\xi = 125 \pm 20$ nm yields the best fit to our experimental data in Fig. 2f (see Supplementary Note 4 for additional details). The calculated LDOS reproduces many of the qualitative features observed in the experiment. The theoretical LB feature at energy $E = -E_0$ in Fig. 2g, for example, persists over the entire region from one domain to the next but has reduced intensity near the interface (that is, for 80 nm < x < 160 nm). The reduction in LB spectral intensity is seen to arise due to one of the three filled sub-bands shifting to higher energy as a result of the valley polarization reversal at the Chern domain interface, consistent with the simple qualitative picture in Fig. 2h. The theoretical UB peak at $E = +E_0$ is completely suppressed at the interface and shifts to $E = 0$ (equivalent to E_F). The downwards-shifting unoccupied sub-band and the upwards-shifting occupied sub-band are seen to merge at $E = 0$ to create 1D chiral modes. The spatial dependence of the theoretical LDOS map at $E = 0$ (Extended Data Fig. 4d) qualitatively reproduces the experimental dI/dV map at $E = E_F$ (Fig. 2e and Extended Data Fig. 4a) and yields a FWHM of the 1D chiral modes of $w = 45$ nm, in reasonable agreement with the experimental value of $w = 57 \pm 10$ nm.

Our combined experimental and theoretical results suggest that chiral interface states arise in tMBLG owing to a gradual transition of the valley polarization across different Chern domains, and we are able to extract a domain wall width of $\xi = 125 \pm 20$ nm that characterizes the length scale of valley reversal in our tMBLG devices. This width, in conjunction with the width of the chiral interface state wavefunction, puts a lower bound on the spacing between chiral channels in future hypothetical devices utilizing tMBLG in order to prevent

inter-channel electronic hybridization. Our treatment suggests the possibility of controlling the width and dispersion of 1D chiral states in tMBLG by engineering the valley domain wall width ξ (see the example in Extended Data Fig. 10). Further reduction of the chiral state width could potentially be realized by creating devices with patterned local gate structures designed to achieve sharper n gradients[26].

In conclusion, our ability to manipulate tMBLG Chern domains and to visualize the resulting 1D chiral interface states provides a method to locally control and characterize topologically non-trivial moiré systems via scanned probe techniques. The creation of Chern domain interfaces decoupled from physical boundaries offers an elegant testbed for theoretical models involving the interplay between strong correlation and non-trivial topology that is devoid of structural defects and edge-mode reconstruction effects. Direct access to the microscopic wavefunction of tMBLG 1D chiral modes enables the characterization of spatially defined topological phase transitions and the extraction of their fundamental length scale, thus providing a means to determine the ultimate limits on device miniaturization involving topologically derived chiral channels. Our capability of creating 1D conducting channels with desired spatial location and chirality can potentially be utilized to build electrically tuneable chiral networks that hold promise for dissipation-free performance[27] and that should facilitate the exploration of exotic topological phenomena[18,19,28].

Online content

Any methods, additional references, Nature Portfolio reporting summaries, source data, extended data, supplementary information, acknowledgements, peer review information; details of author contributions and competing interests; and statements of data and code availability are available at https://doi.org/10.1038/s41567-024-02444-w.

References

1. Trambly de Laissardière, G., Mayou, D. & Magaud, L. Localization of Dirac electrons in rotated graphene bilayers. *Nano Lett.* **10**, 804–808 (2010).
2. Bistritzer, R. & MacDonald, A. H. Moiré bands in twisted double-layer graphene. *Proc. Natl Acad. Sci. USA* **108**, 12233–12237 (2011).
3. Wu, F., Lovorn, T., Tutuc, E. & MacDonald, A. H. Hubbard model physics in transition metal dichalcogenide moiré bands. *Phys. Rev. Lett.* **121**, 026402 (2018).
4. Zhang, Y.-H., Mao, D., Cao, Y., Jarillo-Herrero, P. & Senthil, T. Nearly flat Chern bands in moiré superlattices. *Phys. Rev. B* **99**, 075127 (2019).
5. Liu, J., Ma, Z., Gao, J. & Dai, X. Quantum valley Hall effect, orbital magnetism, and anomalous Hall effect in twisted multilayer graphene systems. *Phys. Rev.* **9**, 031021 (2019).
6. Wu, F., Lovorn, T., Tutuc, E., Martin, I. & MacDonald, A. H. Topological insulators in twisted transition metal dichalcogenide homobilayers. *Phys. Rev. Lett.* **122**, 086402 (2019).
7. Serlin, M. et al. Intrinsic quantized anomalous Hall effect in a moiré heterostructure. *Science* **367**, 900–903 (2020).
8. Polshyn, H. et al. Electrical switching of magnetic order in an orbital Chern insulator. *Nature* **588**, 66–70 (2020).
9. Li, T. et al. Quantum anomalous Hall effect from intertwined moiré bands. *Nature* **600**, 641–646 (2021).
10. Xie, Y. et al. Fractional Chern insulators in magic-angle twisted bilayer graphene. *Nature* **600**, 439–443 (2021).
11. Cai, J. et al. Signatures of fractional quantum anomalous Hall states in twisted $MoTe_2$. *Nature* **622**, 63–68 (2023).
12. Zeng, Y. et al. Thermodynamic evidence of fractional Chern insulator in moiré $MoTe_2$. *Nature* **622**, 69–73 (2023).
13. Park, H. et al. Observation of fractionally quantized anomalous Hall effect. *Nature* **622**, 74–79 (2023).
14. Xu, F. et al. Observation of integer and fractional quantum anomalous Hall effects in twisted bilayer $MoTe_2$. *Phys. Rev.* **13**, 031037 (2023).
15. Polshyn, H. et al. Topological charge density waves at half-integer filling of a moiré superlattice. *Nat. Phys.* **18**, 42–47 (2022).
16. Grover, S. et al. Chern mosaic and Berry-curvature magnetism in magic-angle graphene. *Nat. Phys.* **18**, 885–892 (2022).
17. Tschirhart, C. L. et al. Intrinsic spin Hall torque in a moiré Chern magnet. *Nat. Phys.* **19**, 807–813 (2023).
18. Qi, X.-L., Hughes, T. L. & Zhang, S.-C. Chiral topological superconductor from the quantum Hall state. *Phys. Rev. B* **82**, 184516 (2010).
19. Wang, J., Zhou, Q., Lian, B. & Zhang, S.-C. Chiral topological superconductor and half-integer conductance plateau from quantum anomalous Hall plateau transition. *Phys. Rev. B* **92**, 064520 (2015).
20. Lian, B., Sun, X.-Q., Vaezi, A., Qi, X.-L. & Zhang, S.-C. Topological quantum computation based on chiral Majorana fermions. *Proc. Natl Acad. Sci. USA* **115**, 10938–10942 (2018).
21. Velasco, J. et al. Nanoscale control of rewriteable doping patterns in pristine graphene/boron nitride heterostructures. *Nano Lett.* **16**, 1620–1625 (2016).
22. Park, Y., Chittari, B. L. & Jung, J. Gate-tunable topological flat bands in twisted monolayer-bilayer graphene. *Phys. Rev. B* **102**, 035411 (2020).
23. Rademaker, L., Protopopov, I. V. & Abanin, D. A. Topological flat bands and correlated states in twisted monolayer-bilayer graphene. *Phys. Rev. Res.* **2**, 033150 (2020).
24. Zhang, C. et al. Local spectroscopy of a gate-switchable moiré quantum anomalous Hall insulator. *Nat. Commun.* **14**, 3595 (2023).
25. Středa, P. Quantised Hall effect in a two-dimensional periodic potential. *J. Phys. C.* **15**, L1299–L1303 (1982).
26. Kim, S. et al. Edge channels of broken-symmetry quantum Hall states in graphene visualized by atomic force microscopy. *Nat. Commun.* **12**, 2852 (2021).
27. Zhang, X. & Zhang, S.-C. Chiral interconnects based on topological insulators. in *Proc. SPIE 8373, Micro- and Nanotechnology Sensors, Systems, and Applications IV* (eds by George, T., Islam, M. S. & Dutta, A.) 837309 (2012).
28. Chang, A. M. Chiral Luttinger liquids at the fractional quantum Hall edge. *Rev. Mod. Phys.* **75**, 1449–1505 (2003).

Publisher's note Springer Nature remains neutral with regard to jurisdictional claims in published maps and institutional affiliations.

Springer Nature or its licensor (e.g. a society or other partner) holds exclusive rights to this article under a publishing agreement with the author(s) or other rightsholder(s); author self-archiving of the accepted manuscript version of this article is solely governed by the terms of such publishing agreement and applicable law.

© The Author(s), under exclusive licence to Springer Nature Limited 2024

Methods

Sample preparation

tMBLG samples were prepared using the flip-chip method[29] followed by a forming-gas anneal[30,31]. Electrical contacts were made by evaporating Cr/Au (5 nm/60 nm) through a silicon nitride shadow mask onto the heterostructure. The sample surface cleanliness was confirmed by using contact atomic force microscopy before STM measurements. Samples were annealed at 300 °C overnight in ultra-high vacuum before insertion into the low-temperature STM stage.

STM/STS measurements

All STM/STS measurements were performed in a commercial CreaTec LT-STM held at $T = 4.7$ K using tungsten tips. STM tips were prepared on a Cu(111) surface and calibrated against the Cu(111) Shockley surface state before STS measurements on tMBLG to avoid tip artefacts. dI/dV spectra were recorded using standard lock-in techniques with a small bias modulation of $\Delta V_{\mathrm{RMS}} = 1$ mV at 613 Hz. dI/dV maps were collected by first stabilizing the tip at a higher bias at each position then bringing it closer to the sample surface by a fixed offset ΔZ for measurement (thus allowing the influence of structural corrugation to be minimized). All STM images were edited using WSxM software[32].

Determination of local structural parameters

The moiré superlattice in our topographic images often deviates from exact threefold rotational symmetry owing to the presence of hetero-strain (that is, relatively strain between the stacked graphene monolayer and bilayer). Both the local twist angle and the local hetero-strain were determined via detailed analysis of the moiré pattern[33]. The moiré wavelength was obtained for three directions by measuring the spatial separation between peaks in STM topographs and averaging over several moiré unit cells. The reciprocal primitive vectors $\mathbf{K}_i$ ($i = 0, 1, 2$) were derived through Fourier transform analysis. In the presence of hetero-strain, their magnitude K_i can be approximately written as $K_i = k\left(\theta + (1+\nu_{\mathrm{P}})\epsilon\cos\left(\alpha + i\frac{2\pi}{3}\right)\sin\left(\alpha + i\frac{2\pi}{3}\right)\right)$, where $k = 4.694\ \mathrm{nm}^{-1}$ is the length of a monolayer graphene reciprocal primitive vector, θ is the twist angle, ϵ is the hetero-strain amplitude, $\nu_{\mathrm{P}} = 0.16$ is Poisson's ratio for graphene and α is the angle between the principal axis of the strain tensor and one of the monolayer graphene reciprocal primitive vectors. This allows us to solve for both θ and ϵ from the extracted K_i. Different tMBLG areas shown in this work exhibit variations in local structural parameters (Extended Data Fig. 3), but all display gate-induced topological switching between $C = \pm 2$, consistent with ref. 24. Within a single scan area, the twist angle and hetero-strain are mostly uniform, allowing us to identify charge inhomogeneity as the main cause for the observed spatial variation in gate-dependent dI/dV spectroscopy (see Supplementary Note 1 for details). More detailed analysis methods[34,35] could potentially reveal the presence of fine structural deformations and explain the domain interface pinning/depinning observed in our experiment (see Supplementary Note 3 for details), which we leave for future investigations.

Gaussian fitting of chiral interface state images

For fitting purposes, we assumed that the chiral interface state LDOS is uniform along the domain interface and follows a Gaussian line shape normal to the interface in the plane. We also include a phenomenological constant background term to account for residual dI/dV in the $C = \pm 2$ insulating domains (probably owing to slight doping and/or instrumental broadening). The 1D chiral interface state LDOS can thus be expressed as

$$D(x,y) = D_0 + A\exp\left(-4\ln 2\left(\frac{(x-x_0)\cos\theta + (y-y_0)\sin\theta}{w}\right)^2\right),$$

where D_0 is the constant background, A is the maximum intensity of the Gaussian peak, (x_0, y_0) defines the interface, θ is the angle between the normal to the interface and the x axis and w is the Gaussian FWHM. Extended Data Fig. 6a,c,e,g shows experimental dI/dV maps obtained in four different tMBLG areas (1–4), and Extended Data Fig. 6b,d,f,h shows the corresponding fits. The FWHM values extracted for different data sets are summarized in Extended Data Fig. 6i and have an average width of $w = 57 \pm 10$ nm $\approx 5l_{\mathrm{M}}$, where l_{M} is the moiré wavelength. w exhibits some slight variation for different electron density gradients and B fields, but the exact relationship is not yet determined beyond the parameter regime presented here.

Data availability

Additional data are available from the corresponding authors upon request. Source data are provided with this paper.

Code availability

The computer codes that support the plots within this paper and the findings of this study are available from the corresponding authors upon request.

References

29. Cui, X. et al. Low-temperature ohmic contact to monolayer MoS_2 by van der Waals bonded Co/h-BN electrodes. *Nano Lett.* **17**, 4781–4786 (2017).
30. Garcia, A. G. F. et al. Effective cleaning of hexagonal boron nitride for graphene devices. *Nano Lett.* **12**, 4449–4454 (2012).
31. Au-Jung, H. S. et al. Fabrication of gate-tunable graphene devices for scanning tunneling microscopy studies with Coulomb impurities. *JoVE* **24**, e52711 (2015).
32. Horcas, I. et al. WSXM: a software for scanning probe microscopy and a tool for nanotechnology. *Rev. Sci. Instrum.* **78**, 013705 (2007).
33. Kerelsky, A. et al. Maximized electron interactions at the magic angle in twisted bilayer graphene. *Nature* **572**, 95–100 (2019).
34. Benschop, T. et al. Measuring local moiré lattice heterogeneity of twisted bilayer graphene. *Phys. Rev. Res.* **3**, 013153 (2021).
35. de Jong, T. A. et al. Imaging moiré deformation and dynamics in twisted bilayer graphene. *Nat. Commun.* **13**, 70 (2022).

Acknowledgements

The authors thank Y.-M. Lu for helpful discussion and S. Stolz for technical support. This research was primarily supported by the US Department of Energy, Office of Science, Office of Basic Energy Sciences, Materials Sciences and Engineering Division under contract no. DE-AC02-05CH11231 within the van der Waals Heterostructures programme KCWF16 (STM spectroscopy). Work at the Molecular Foundry (graphene characterization) was supported by the US Department of Energy, Office of Science, Office of Basic Energy Sciences under contract no. DE-AC02-05CH11231. Support was also provided by the National Science Foundation Award DMR-2221750 (device fabrication and testing). K.W. and T.T. acknowledge support from JSPS KAKENHI (grant nos. 20H00354, 21H05233 and 23H02052) and World Premier International Research Center Initiative (WPI), MEXT, Japan (hBN crystal synthesis and characterization). C.Z. acknowledges support from a Kavli ENSI Philomathia Graduate Student Fellowship. T.S. acknowledges fellowship support from the Masason Foundation.

Author contributions

C.Z., T.Z. and M.F.C. initiated and conceived the research. C.Z. and T.Z. carried out STM/STS measurements and analyses. M.F.C. supervised STM/STS measurements and analyses. S.K. prepared gate-tuneable devices. A.Z., F.W. and M.F.C. supervised device preparations. T.S. performed theoretical analysis and calculations. M.P.Z. supervised theoretical analysis and calculations. T.T. and K.W. provided the hBN crystals. C.Z., T.Z. and M.F.C. wrote the manuscript with the help of all authors. All authors contributed to the scientific discussion.

Competing interests

The authors declare no competing interests.

Additional information

Extended data is available for this paper at https://doi.org/10.1038/s41567-024-02444-w.

Supplementary information The online version contains supplementary material available at https://doi.org/10.1038/s41567-024-02444-w.

Correspondence and requests for materials should be addressed to Tiancong Zhu or Michael F. Crommie.

Peer review information *Nature Physics* thanks Tjerk Benschop and the other, anonymous, reviewer(s) for their contribution to the peer review of this work.

Reprints and permissions information is available at www.nature.com/reprints.

https://doi.org/10.1038/s41567-024-02444-w

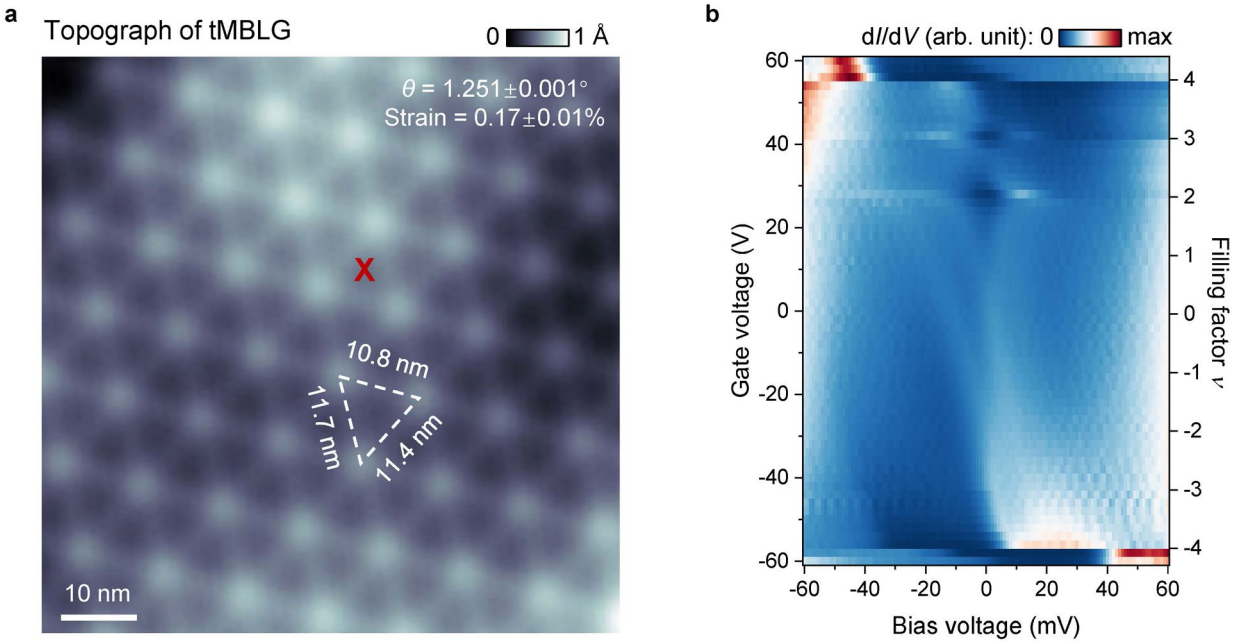

Extended Data Fig. 1 | Basic STM/STS characterization of gate-tuneable tMBLG. a, STM topographic image of a tMBLG device surface area ($V_{Bias} = -200$ mV, setpoint $I_0 = 2$ nA). Analysis of the moiré wavelength in all three directions enables the extraction of a local twist angle of $\theta = 1.251 \pm 0.001°$ and a local hetero-strain of $0.17 \pm 0.01\%$ (Methods). **b**, Gate-dependent dI/dV density plot over the full range $-70\ \text{V} \leq V_G \leq 70\ \text{V}$ ($-4.3 \leq \nu \leq 4.3$) obtained for STM tip at the location marked in **a** (modulation voltage $\Delta V_{RMS} = 1$ mV; setpoint $V_{Bias} = -100$ mV, $I_0 = 2$ nA). Charge gaps emerging at $\nu = 2, 3$ signify the formation of correlated insulating states. All measurements taken at $T = 4.7$ K.

https://doi.org/10.1038/s41567-024-02444-w

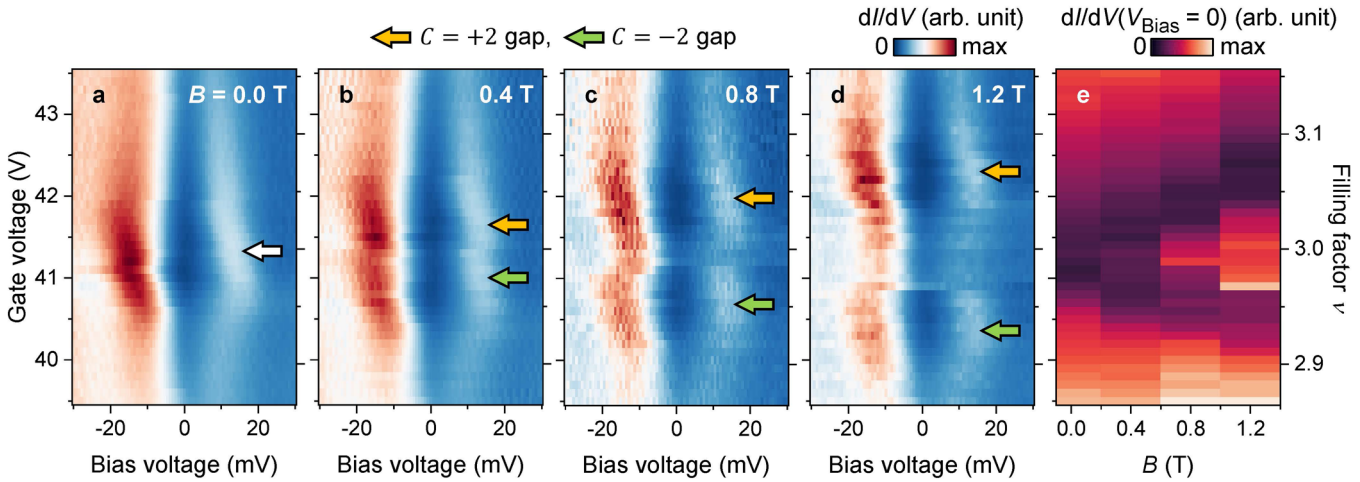

Extended Data Fig. 2 | Topological behaviour of tMBLG QAH states in an out-of-plane *B*-field. a–**d**, Gate-dependent d*I*/d*V* density plots near $\nu = 3$ for **a** $B = 0.0$ T, **b** $B = 0.4$ T, **c** $B = 0.8$ T, and **d** $B = 1.2$ T (modulation voltage $\Delta V_{RMS} = 1$ mV; setpoint $V_{Bias} = -75$ mV, $I_0 = 0.2$ nA). The white arrow indicates the energy gap for $B = 0.0$ T, and orange and green arrows indicate $C = +2$ and $C = -2$ gaps for finite B. **e**, d*I*/d*V*($V_{Bias} = 0$) as a function of V_G and *B*-field extracted from **a**–**d** (same data as in Fig. 1f but without dashed lines).

https://doi.org/10.1038/s41567-024-02444-w

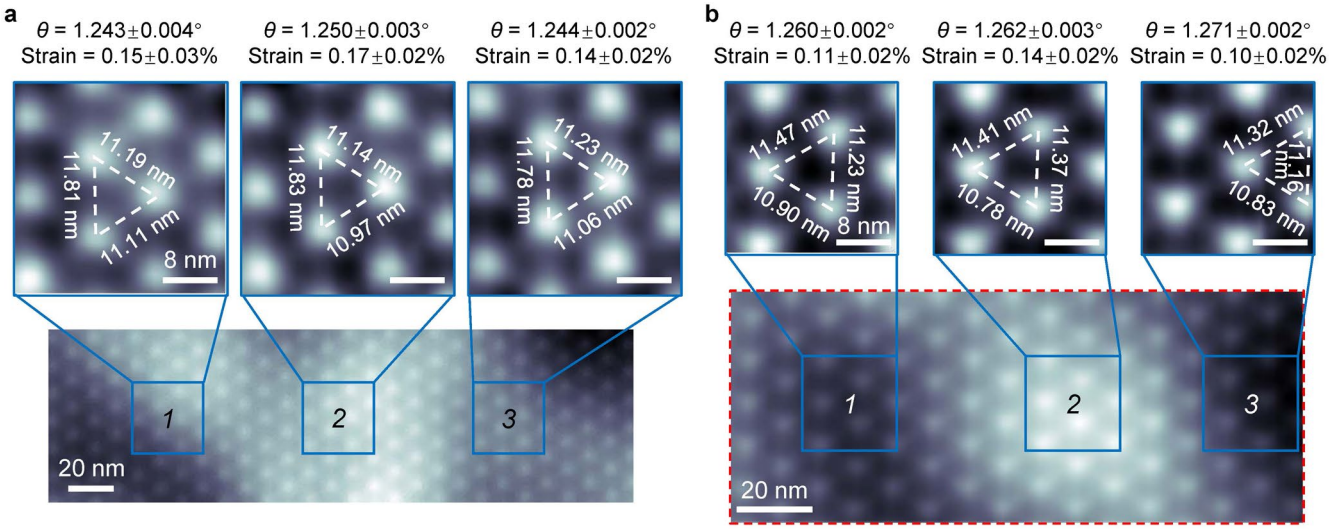

Extended Data Fig. 3 | Local twist angle and hetero-strain of tMBLG areas with Chern domain interfaces. a, STM topographic image of a tMBLG area with a Chern domain interface (V_{Bias} = −300 mV, setpoint I_0 = 0.2 nA; same as Fig. 2a). Local moiré wavelengths in three different directions are shown for locations *1*, *2*, and *3* from which local twist angle and hetero-strain values are extracted (Methods). **b**, STM topographic image of another tMBLG area with a Chern domain interface after quantum dot creation (V_{Bias} = −1 V, setpoint I_0 = 0.01 nA; same as Fig. 4a boxed region). A similar structural analysis is shown.

https://doi.org/10.1038/s41567-024-02444-w

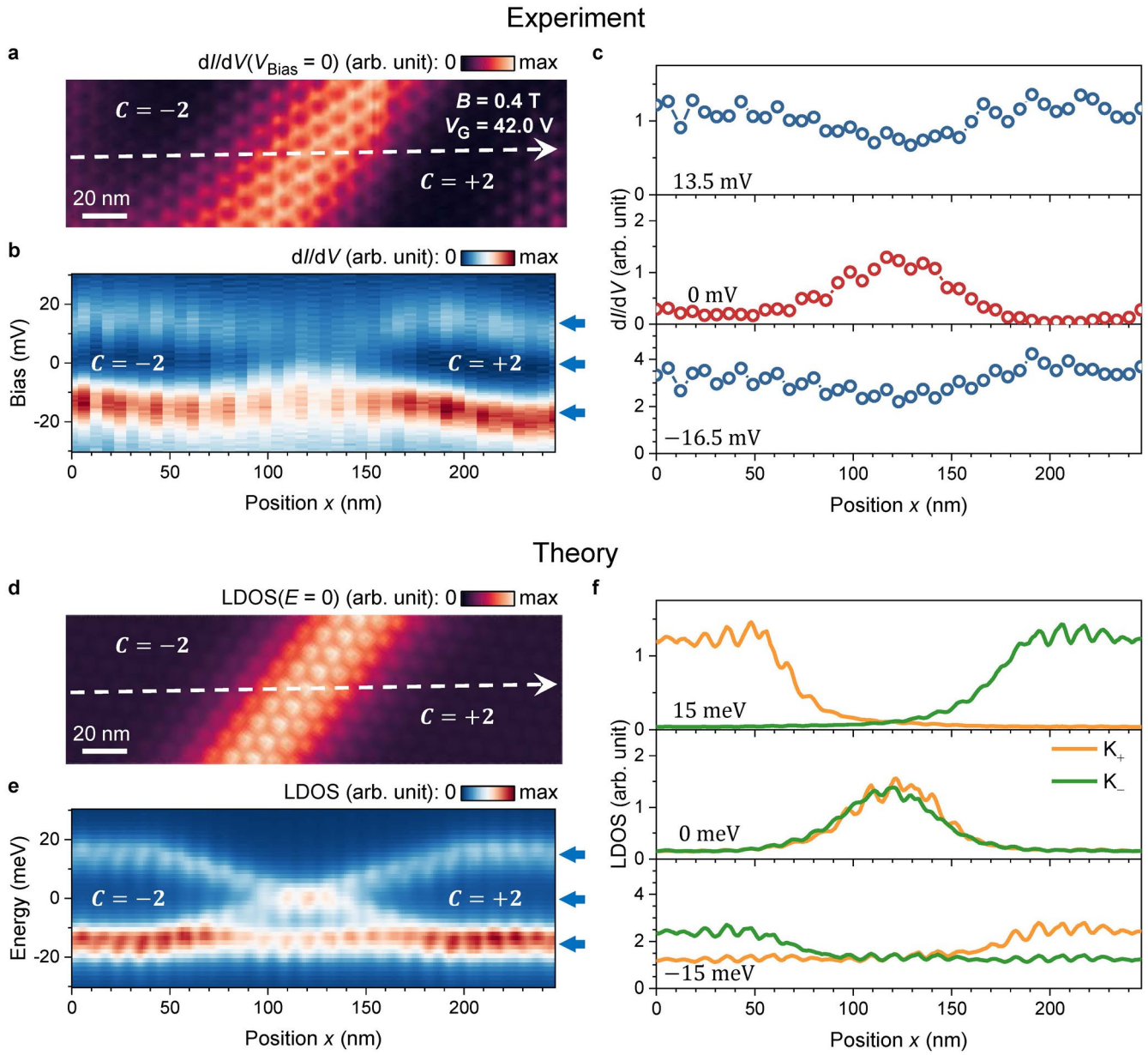

Extended Data Fig. 4 | Experiment–theory comparison for topological phase transition and chiral interface states. a, d*I*/d*V* map of a tMBLG area for $B = 0.4$ T, $V_G = 42.0$ V, and $V_{Bias} = 0$ mV (same as Fig. 2e). **b**, d*I*/d*V* density plot for $B = 0.4$ T and $V_G = 42.0$ V obtained along the white dashed line in **a** (same as Fig. 2f). **c**, d*I*/d*V* spatial line-cuts extracted from **b** at $V_{Bias} = 13.5$ mV (top), 0 mV (middle), and −16.5 mV (bottom) (corresponding to blue arrows in **b**). **d**, Theoretical LDOS map for $E = 0$ meV calculated for a tMBLG Chern domain wall width of $\xi = 125$ nm. **e**, Density plot of theoretical LDOS along the white dashed line in **d** (same as Fig. 2g). **f**, Valley-resolved theoretical LDOS line-cuts at $E = 15$ meV (top), 0 meV (middle), and −15 meV (bottom) (corresponding to blue arrows in **e**).

https://doi.org/10.1038/s41567-024-02444-w

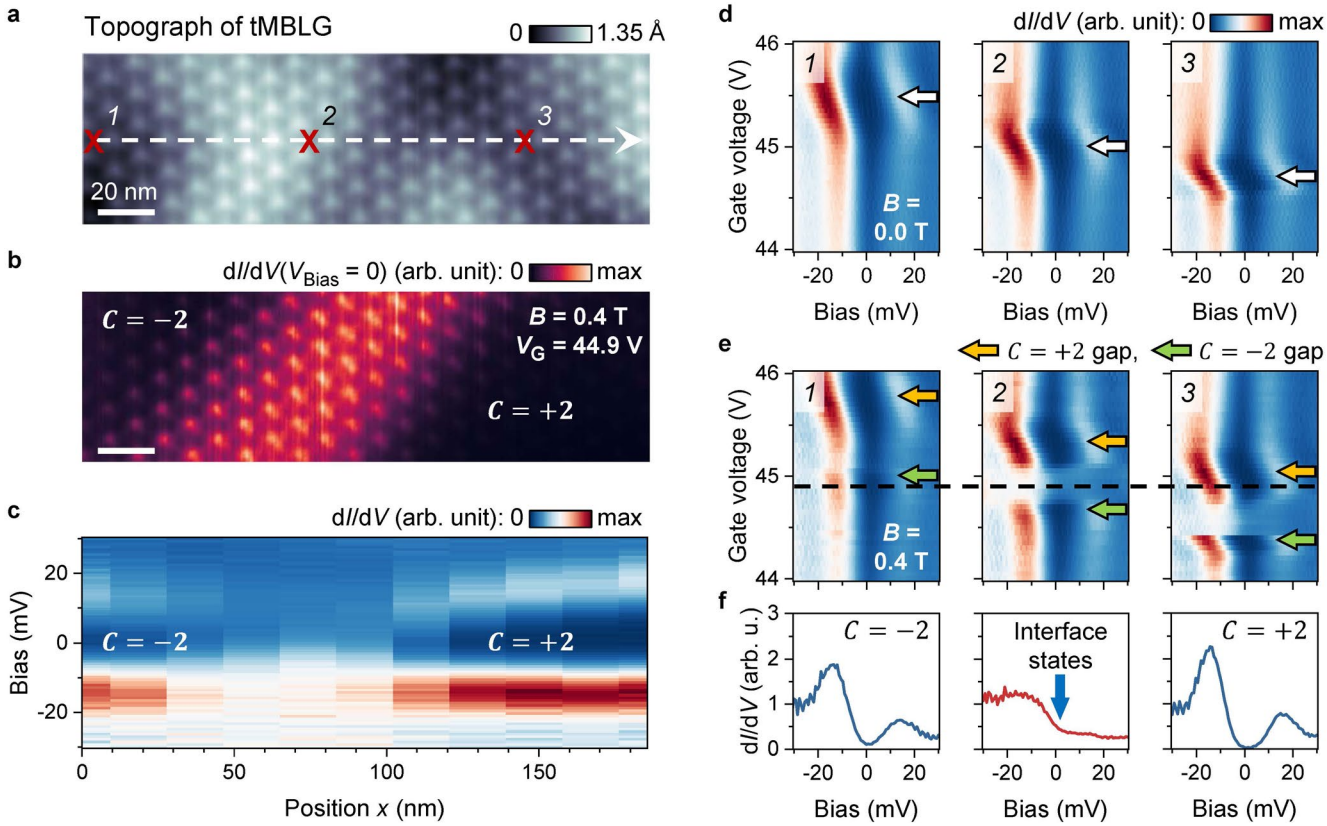

Extended Data Fig. 5 | Spatially-defined topological phase transition and chiral interface states for a different area. a, STM topographic image of a different tMBLG area (V_{Bias} = −300 mV, setpoint I_0 = 0.2 nA). **b**, d*I*/d*V* map of the same area as **a** for B = 0.4 T, V_G = 44.9 V and V_{Bias} = 0 mV. **c**, d*I*/d*V* density plot for B = 0.4 T and V_G = 44.9 V obtained along the white dashed line in **a**. **d**, Gate-dependent d*I*/d*V* density plots for B = 0.0 T obtained at locations *1*, *2*, and *3* marked in **a**. White arrows indicate the ν = 3 energy gap. **e**, Same as **d**, but for B = 0.4 T. Orange and green arrows indicate C = +2 and C = −2 gaps. **f**, d*I*/d*V* spectra for B = 0.4 T and V_G = 44.9 V at locations *1*, *2*, and *3* of **a**. Spectroscopy parameters: modulation voltage ΔV_{RMS} = 1 mV; setpoint V_{Bias} = −60 mV, I_0 = 0.5 nA for **d**, **e**; setpoint V_{Bias} = −300 mV, I_0 = 0.2 nA and tip height offset ΔZ = −0.2 nm for **b**, **c**, **f**.

https://doi.org/10.1038/s41567-024-02444-w

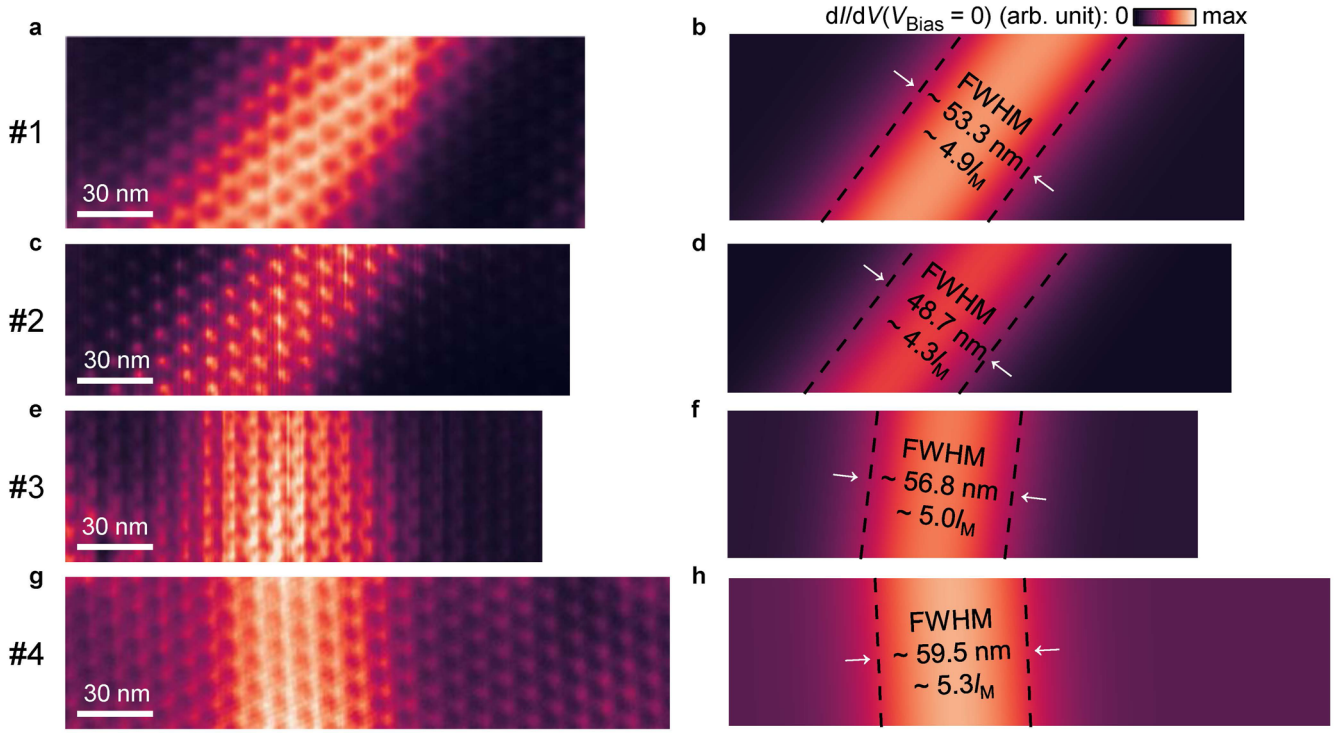

i

Area	*n*-gradient (10^8 cm^{-2}/nm)	Origin of *n*-gradient	*B* (T)	V_G (V)	FWHM (nm)
#1	3.2	Naturally occurring	0.4	41.9 (inc.) 42.0 (inc.) 42.1 (inc.) 42.1 (dec.) 42.0 (dec.) 41.9 (dec.)	51.7 52.5 56.2 55.1 53.3 52.2
#2	4.4	Naturally occurring	0.4	45.0 (dec.) 44.9 (dec.) 44.8 (dec.) 44.7 (dec.)	51.5 48.7 46.9 40.7
#3	3.2	STM tip-pulse-induced quantum dot	0.4 0.3	42.0 (dec.)	59.5 56.8
#4	3.9	STM tip-pulse-induced quantum dot	0.3 0.2	42.1 (dec.)	59.5 66.6

Extended Data Fig. 6 | Fitting the spatial profile of chiral interface states. **a**, Experimental d*I*/d*V* map showing 1D chiral interface states obtained in area #1 for $B = 0.4$ T, $V_G = 42.0$ V and $V_{Bias} = 0$ mV (same as Fig. 2e). **b**, 2D fit to image in **a** with a Gaussian peak and a constant background (see Methods). **c**, Experimental d*I*/d*V* map showing 1D chiral interface states obtained in area #2 for $B = 0.4$ T, $V_G = 44.9$ V and $V_{Bias} = 0$ mV (Same as Extended Data Fig. 5b). **d**, 2D fit to image in **c** with a Gaussian peak and a constant background (see Methods). **e**, Experimental d*I*/d*V* map showing 1D chiral interface states obtained in area #3 for $B = 0.3$ T, $V_G = 42.0$ V and $V_{Bias} = 0$ mV. **f**, 2D fit to image in **e** with a Gaussian peak and a constant background (see Methods). **g**, Experimental d*I*/d*V* map showing 1D chiral interface states obtained in area #4 for $B = 0.3$ T, $V_G = 42.1$ V and $V_{Bias} = 0$ mV. **h**, 2D fit to image in **g** with a Gaussian peak and a constant background (see Methods). **i**, Summary of 2D Gaussian fitting for datasets from areas #1–4. inc. = increasing gate voltage; dec. = decreasing gate voltage.

https://doi.org/10.1038/s41567-024-02444-w

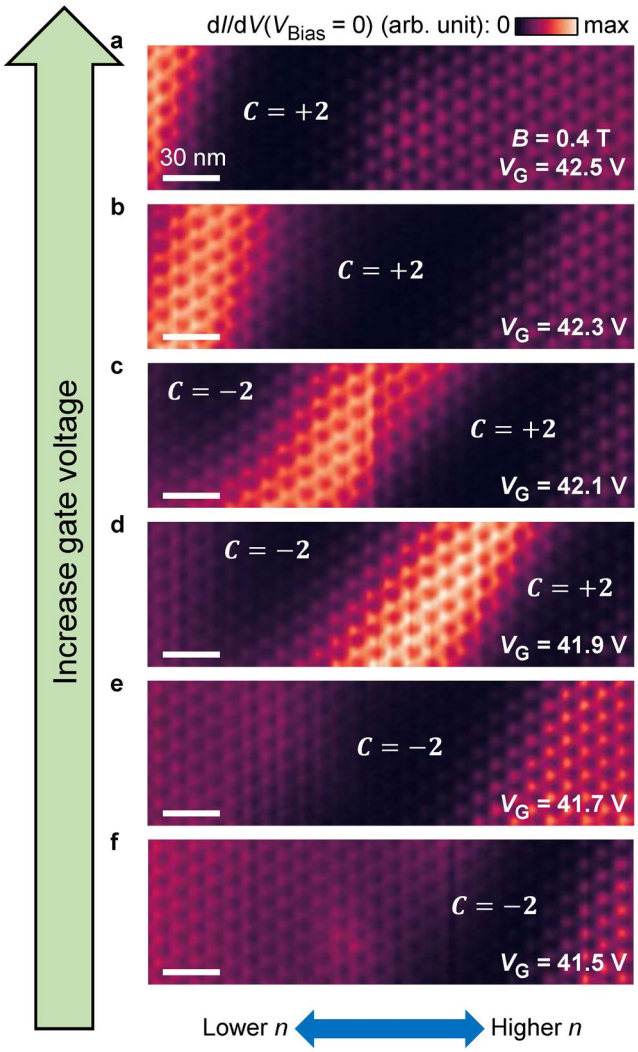

Extended Data Fig. 7 | Reversible displacement of chiral interface states via back-gating. a–f, d*I*/d*V* maps of the same area as Fig. 2a at $B = 0.4$ T and $V_{Bias} = 0$ mV for **a** $V_G = 42.5$ V, **b** $V_G = 42.3$ V, **c** $V_G = 42.1$ V, **d** $V_G = 41.9$ V, **e** $V_G = 41.7$ V, and **f** $V_G = 41.5$ V. Modulation voltage $\Delta V_{RMS} = 1$ mV; setpoint $V_{Bias} = -300$ mV, $I_0 = 0.2$ nA; tip height offset $\Delta Z = -0.075$ nm.

https://doi.org/10.1038/s41567-024-02444-w

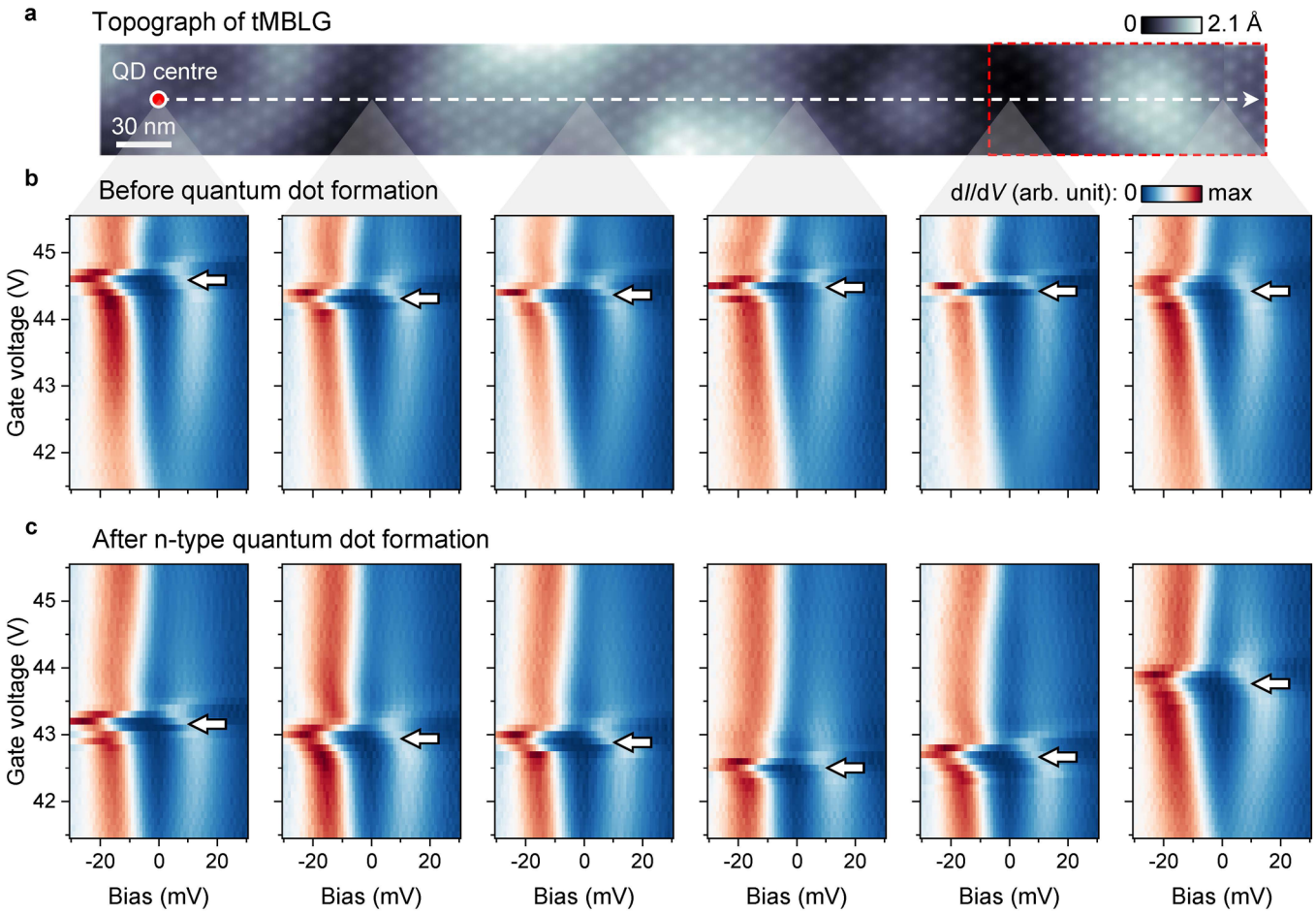

Extended Data Fig. 8 | Local electron density profile of an n-type quantum dot. a, STM topographic image of a tMBLG area ($V_{Bias} = -1$ V, setpoint $I_0 = 0.01$ nA; same as Fig. 4a). **b**, Representative gate-dependent dI/dV density plots for $B = 0.0$ T obtained at different locations indicated on white dashed line of **a**. The $\nu = 3$ gap (white arrows) always appears near $V_G = 44.3$ V, indicating a low variation of local electron density over the entire area in **a** ($\Delta\nu < 0.02$). **c**, Representative gate-dependent dI/dV density plots for $B = 0.0$ T obtained at the same locations as in **b** after the formation of an n-type quantum dot. A significant electron density gradient occurs in the rightmost region (highlighted by the red dashed box in **a**) where a Chern domain interface hosting 1D chiral states can be realized (Fig. 4c). Spectroscopy parameters: modulation voltage $\Delta V_{RMS} = 1$ mV; setpoint $V_{Bias} = -60$ mV, $I_0 = 0.5$ nA.

https://doi.org/10.1038/s41567-024-02444-w

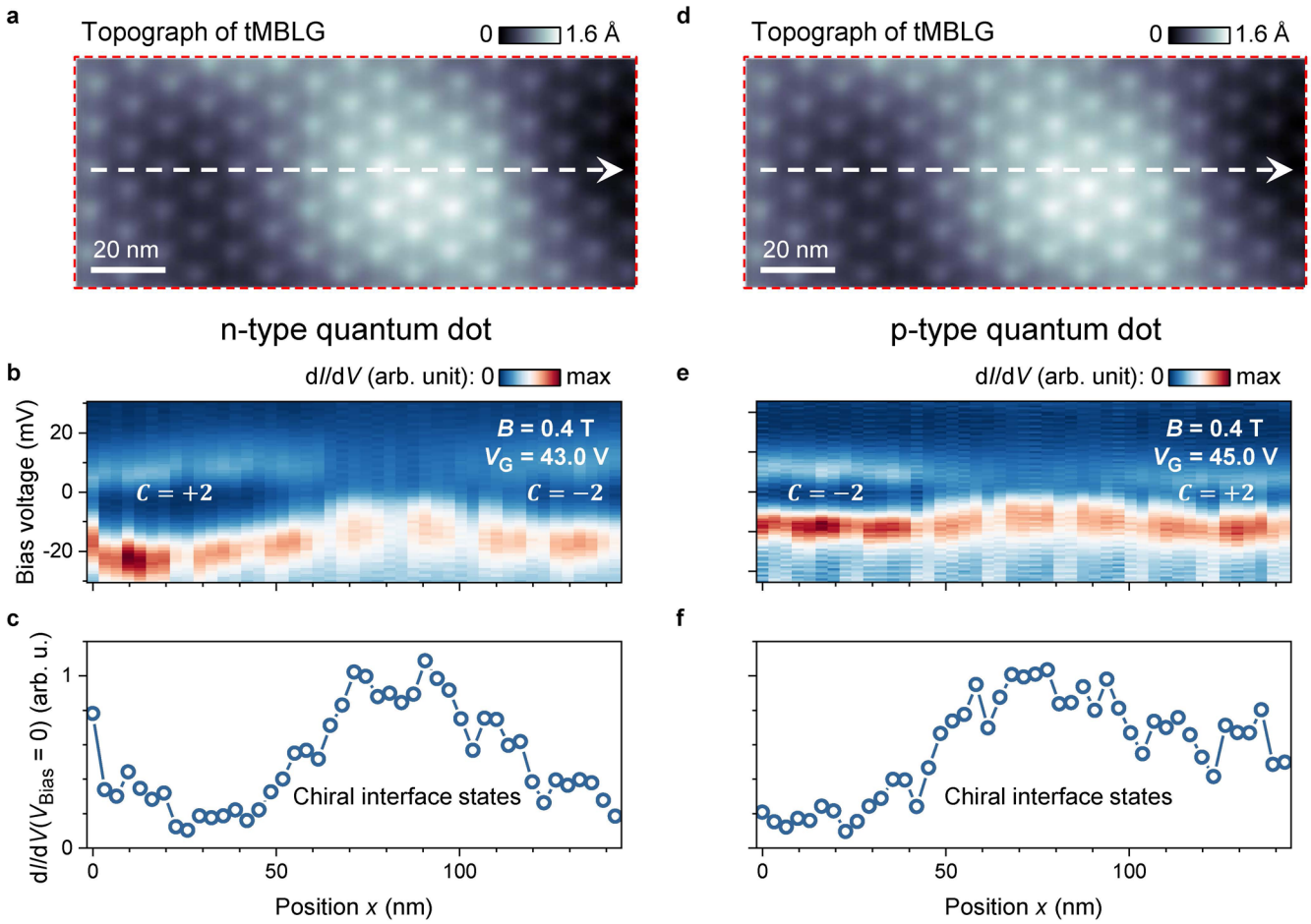

Extended Data Table. 9 | Spatially-defined topological phase transition and 1D chiral states at quantum-dot-generated Chern domain interfaces. **a**, Zoom-in STM topographic image of the boxed region shown in Fig. 4a (V_{Bias} = −1 V, setpoint I_0 = 0.01 nA). **b**, dI/dV density plot for B = 0.4 T and V_G = 43.0 V obtained along the white dashed line in **a** after formation of an n-type quantum dot (modulation voltage ΔV_{RMS} = 1 mV; setpoint V_{Bias} = −300 mV, I_0 = 0.2 nA; tip height offset ΔZ = −0.075 nm). Charge gaps in the left and right regions are attributed to the C = +2 and C = −2 insulating states. The absence of a gap in the middle signifies the presence of chiral interface states. **c**, dI/dV spatial line-cut at V_{Bias} = 0 mV extracted from **b**. **d**–**f**, Same as **a**–**c**, but after formation of a p-type quantum dot. Charge gaps in the left and right regions are attributed to the C = −2 and C = +2 insulating states. The absence of a gap in the middle signifies the presence of chiral interface states.

https://doi.org/10.1038/s41567-024-02444-w

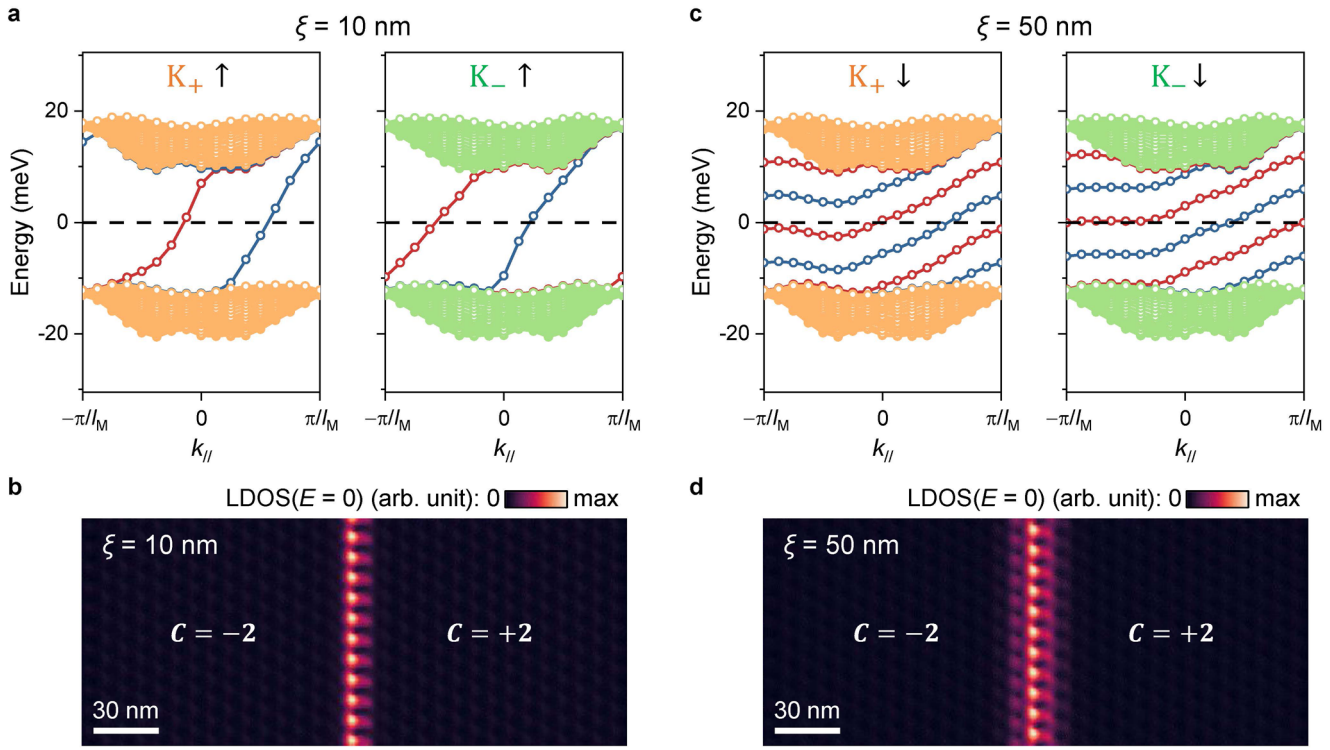

Extended Data Table. 10 | 1D band structure and chiral state image for a tMBLG Chern domain interface. a, Energy eigenvalues as a function of momentum along the interface ($k_{||}$) calculated for a Chern domain wall width of $\xi = 10$ nm (the minimum value allowed in our model). Only electronic states for spin up are shown (corresponding to the sub-bands in Fig. 2h that shift upward/downward). Two branches of chiral interface states (marked by red and blue) emerge for each valley that connect the occupied and unoccupied bulk bands (thus spanning the bulk gap) and disperse unidirectionally in momentum. The total number of chiral modes (four) is equal to the Chern number difference between neighbouring domains. **b**, Theoretical LDOS map for $E = 0$ meV showing a FWHM of $w = 9$ nm for the 1D chiral interface modes arising from a Chern domain wall width of $\xi = 10$ nm. **c**, Energy eigenvalues calculated for a larger $\xi = 50$ nm. Here more in-gap eigenstates appear at a given momentum, but the number of chiral branches crossing E_F (dashed lines) remains the same (two per valley, marked by red and blue). This is because the group velocity of interface modes becomes smaller (see Supplementary Note 4 for details) so they now extend over more than one Brillouin zone in momentum. **d**, Theoretical LDOS map for $E = 0$ meV showing a FWHM of $w = 17$ nm for the 1D chiral interface modes arising from a Chern domain wall width of $\xi = 50$ nm.